J. Fluid Mech. (2000), *vol.* 419, *pp.* 263–282. Printed in the United Kingdom

Patterns of bubble desorption during the solidification of a multicomponent melt

By M. A. ROGERSON AND S. S. S. CARDOSO

Department of Chemical Engineering, University of Cambridge
Pembroke Street, Cambridge CB2 3RA, UK

(Received 10 June 1999 and in revised form 15 February 2000)

The desorption of bubbles during solidification of a melt occurs in processes as diverse as the making of ice cubes, the formation of igneous rocks and the casting of metals. In both the metal casting and rock formation processes, careful observation of the final solid suggests that the desorbed bubbles often form regular spatial patterns. Understanding and quantifying the mechanisms by which such patterns arise is important. In the geological context, comparison between field measurements and the predictions of a model will allow geologists to estimate *in-situ* magma properties. In the metal casting context, engineers would like to be able to specify mould geometries and cooling conditions to ensure that the distribution of bubbles will not compromise the strength of critical sections of the casting.

In the present study, we develop a detailed mathematical model to predict the distribution of desorbed bubbles in a solidified melt. Our new model builds upon previous knowledge on this phenomenon in the geological context (Toramaru *et al.* 1996, 1997). We describe desorption of a dissolved gas in a semi-infinite melt, solidified by a one-dimensional heat flux. In the absence of convection, the transfer of heat and solute occurs mainly by a diffusive mechanism and the crystallization proceeds most rapidly near the cooled boundary. The crystals formed contain almost no dissolved gas and hence the concentration of gas dissolved in the melt increases progressively towards the cooled boundary. Diffusion of dissolved gas from the crystallizing zone is slow and, as a result, the local melt becomes supersaturated and gas bubbles desorb. The full equations for this coupled solidification and desorption processes are solved numerically.

We find that bubbles desorb forming a sequence of layers parallel to the cooled boundary. The spacing between these bubble layers increases geometrically from the cooled boundary. We give a physical interpretation for this geometric pattern and analyse the effect of physical parameters on the layer spacing. We show that our theoretical model captures the important physical mechanisms involved in the solidification and desorption processes by comparing its predictions with available measurements from a geological formation.

1. Introduction

The casting of steel is one of the most important industrial processes where desorption of bubbles occurs (figure 1*a*). Prior to casting, substantial amounts of oxygen from the basic oxygen steel-making process can dissolve in the molten metal, as well as smaller amounts of other gases such as nitrogen or hydrogen. These dissolved gases can be removed from the molten metal prior to casting by procedures

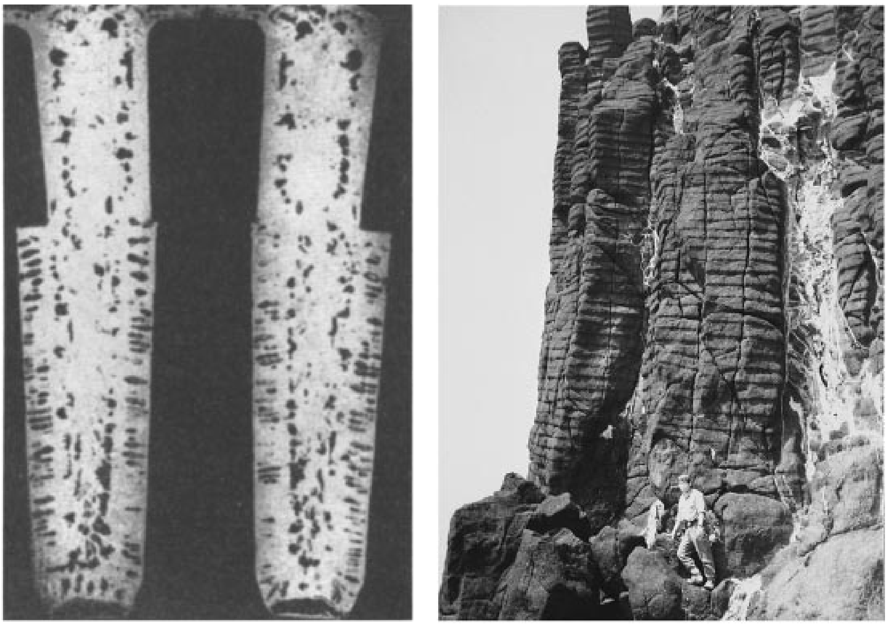
(*a*) (*b*)

FIGURE 1. (*a*) Bubbles of nitrogen desorbed during solidification of a chromium steel ingot (from Carney 1953). Reprinted with permission from ASM International. (*b*) Bubble layers in the Ogi picrite sill (from Toramaru *et al.* 1996). The spacing between the layers is about 20 cm. Reprinted with permission from Springer-Verlag.

such as vacuum degassing or reaction with added deoxidizing compounds to form solid precipitates. However, these procedures must be carefully controlled as without some bubble desorption during solidification, mould shrinkage can occur (Campbell 1991). Shrinkage of the molten metal within the mould occurs as it solidifies because of the greater density of solid to molten metal. It can cause the metal to tear away from the mould walls resulting in a deformed casting. The formation and expansion of gas bubbles during solidification can offset this shrinkage. It is therefore important to be able to specify the dissolved gas concentration, based on mould geometry and cooling conditions, to ensure that the distribution of bubbles in the solid will offset shrinkage, without compromising the strength of critical sections of the casting.

The desorption of bubbles during the solidification of a melt occurs in many other processes, from the day to day making of ice cubes to the formation of igneous rocks. Most of our present knowledge on the mechanism of bubble desorption during solidification has been developed in the geological context. In certain rock formations, such as the Ogi picrite sill on the coast of Sado Island, Japan (figure 1*b*) bubbles were formed during solidification as water originally dissolved in the molten rock desorbed in the form of water vapour.

In both the metal casting and rock formation processes described above, careful observation of the final solid suggests that the desorbed bubbles often form regular spatial patterns. This is particularly clear in the geological example, where the bubbles form layers which lie parallel to the cooled boundary and the spacing between the layers increases in a geometric fashion from the cooled boundary.

Similar periodic patterns have been found in solid precipitate systems where no solidification takes place. For example, Liesegang rings may be observed by placing

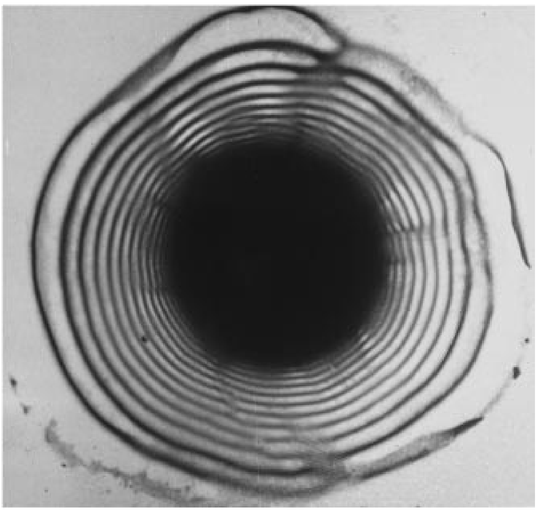

FIGURE 2. Liesegang rings, formed when a small crystal of silver nitrate is placed into a dilute solution of potassium dichromate in gelatin (from McBirney & Noyes 1979). The diameter of the outer rings is about 5 cm. Reprinted with permission from Oxford University Press.

a crystal of silver nitrate into a dilute solution of potassium dichromate in gelatin. Concentric rings of precipitated silver chromate are observed to form progressively from the crystal, the spacing increasing geometrically between each ring (figure 2). Several theories have been proposed to explain this phenomenon but we shall only mention here the supersaturation theory of Ostwald as it is relevant to the development of our model (see for example Stern 1953). Ostwald proposed that the periodicity arises from the interplay between the diffusion of silver ions from the surface of the crystal and the diffusion of chromate ions originally dispersed uniformly in the gelatin, as well as the rate of precipitation. Wagner (1950) modelled this process assuming that precipitation occurs when the product of the two ionic concentrations exceeds a certain value, thus forming a mass sink towards which the ions diffuse. His model was able to predict the geometrical spacing of the layers. The same type of model was used by McBirney & Noyes (1979) to describe the mechanism by which alternate layers of precipitates form in igneous rocks. These layers are oriented parallel to the cooled boundary and the layer spacing increases from this boundary. This suggested that the layers could have arisen in an analogous manner to Liesegang rings, but from the interplay between the diffusivities of a dissolved component and of heat. Complete precipitation of this component was assumed to occur when its concentration was sufficiently high and the temperature sufficiently low. They were able to show that their predicted layer spacings were consistent with field measurements. The problem of bubble desorption during solidification is, however, different from these precipitating systems, because bubble desorption occurs as a result of concentration enrichment during solidification (see § 2).

Previous modelling work on bubble desorption during solidification was developed in analogy to the models for these precipitating systems. Toramaru *et al.* (1996) considered the mechanism by which layers of bubbles such as those observed in figure 1(*b*) were formed. These authors asserted that bubble nucleation occurs at a sufficiently high concentration of the dissolved gas and a sufficiently low temperature. This model is based on a scaling analysis and does not couple the processes of concentration enrichment and diffusion. The model describes qualitatively the geometric layer spacing observed in a number of geological formations. However, the effects of fluid properties and of cooling rate of the patterns of bubble desorption are not considered.

In the present study, we develop a detailed mathematical model to predict the distribution of desorbed bubbles in a solidified melt. In § 2, we describe the physical mechanism of bubble desorption during solidification. In § 3, we develop a new model, which builds upon and extends the scaling analysis of Toramaru *et al.* (1996, 1997). A physical interpretation of the patterns of bubbles in the solid and an analysis of the effect of physical parameters on the layer spacing is given in § 4. In § 5, the new theoretical model is shown to capture the important physical mechanisms involved in the solidification and desorption processes by comparing its predictions with available measurements from a geological formation. Final conclusions on the work are drawn in § 6.

2. Mechanism of bubble desorption during solidification

Consider the cooling of a multicomponent melt, such as a metal alloy, containing a dissolved gas, e.g. oxygen, by removing heat from its boundaries to induce solidification. Crystals, which contain a smaller fraction of dissolved gas than was present in the original liquid, will begin to form. During the initial stages of cooling, the melt convects turbulently, as the Rayleigh number,

$$Ra = \frac{g\xi \Delta T d^3}{\nu\kappa}, \tag{2.1}$$

is large owing to the large temperature difference between the cooled boundary and the melt, ΔT, and the relatively low kinematic viscosity of the melt, ν. Here, g is the acceleration due to gravity, ξ is the coefficient of thermal expansion of the fluid, d is the depth of fluid and κ is the thermal diffusivity of the fluid. As cooling proceeds, the Rayleigh number decreases, mainly as a result of the increasing viscosity due to the presence of crystals. We shall see later that the transition from fully turbulent convection to a quiescent regime occurs over very narrow ranges of temperature and concentration. During the convecting regime, the fluid is well mixed and the concentration and temperature are both uniform. We assume that a chilled layer of solid does not form on the cooled boundary during convection. This would be the case if, for example, the temperature of the boundary is sufficiently high, or convection sufficiently strong. During the quiescent regime, diffusion is the dominant mechanism of heat and solute transfer. We assume that once the melt becomes quiescent, the concentration of dissolved gas is c_o (figure 3*a*).

As cooling proceeds, a layer of solid is progressively formed from the top boundary. As the melt is multicomponent, we assume that ahead of this solid layer is a mushy zone where the crystal fraction decreases gradually from one to the crystal fraction in the bulk of the melt (Kurz & Fisher 1986). The concentration of dissolved gas in the liquid thus increases progressively towards the cooled boundary (figure 3*b*). If the diffusion of dissolved gas from the crystallizing zone is sufficiently slow, then the local melt can become sufficiently supersaturated for gas bubbles to nucleate, say at concentration c^* at the local temperature (figure 3*c*). We assume that the volume fraction of crystals upon bubble nucleation is sufficiently high that the bubbles are prevented from subsequent buoyant motion.

Upon bubble nucleation, the concentration of dissolved gas in the melt in contact with the bubbles is reduced to the saturation concentration at the local temperature

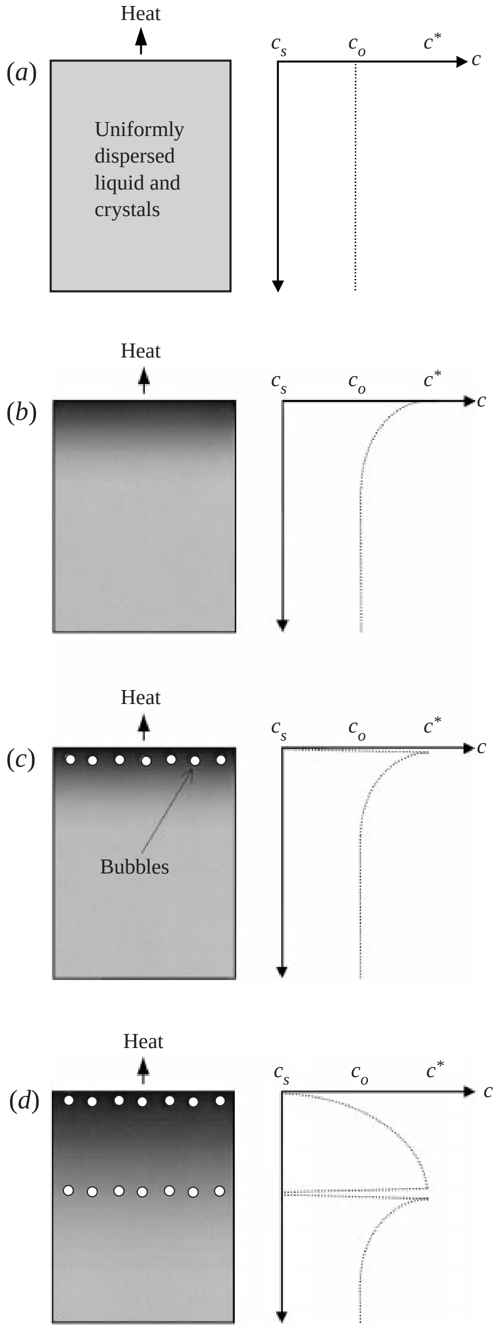

FIGURE 3. The periodic desorption of bubbles. (*a*) The convecting melt becomes stagnant. (*b*) The concentration of dissolved gas, *c*, increases towards the cooled surface because of concentration enrichment. The shade indicates that the fraction of crystals decreases from the cooled boundary. (*c*) The concentration of dissolved gas becomes high enough for gas bubbles to nucleate. The concentration of dissolved gas in the vicinity is reduced to the saturation concentration at this temperature. (*d*) The dissolved gas ahead of the bubbles diffuses back into them creating a region depleted of dissolved gas. At some later position, another burst of bubble nucleation takes place.

c_s. In § 3, c_s is assumed to be lower than c_o as a result of the concentration enrichment that took place during the initial convecting stage of the process.

A gradient of dissolved gas concentration thus develops: c varies from c_s at the bubble surface, through a maximum, to c_o at large distances from the nucleated bubbles. The dissolved gas will therefore diffuse towards and then into the bubbles. As a result, a region depleted of dissolved gas grows ahead of the bubbles. The front of this region initially advances faster than the cooling front because of its closer proximity to the mass sink – the nucleated bubbles – than to the heat sink – the cooled boundary. At steady state, no further nucleation can take place until the cooling front overtakes the gas depletion front. Then a new burst of bubble nucleation will occur and the process will be repeated (figure 3*d*).

Subsequent bursts of bubble nucleation will occur further from each other due to the heat sink becoming further away with each burst whilst the relative position of the mass sink remains fixed. A pattern of discrete bursts of bubble nucleation may thus arise. This physical mechanism relies on the establishment of a gradient of dissolved gas concentration in the melt and diffusion as the dominant transport mechanism.

In the next section, we develop a full mathematical model for the solidification and desorption processes. The temperature and concentration fields are determined by the equations for diffusion of heat and the dissolved gas, with source and sink terms to take into account concentration enrichment and latent heat effects.

3. Modelling

We shall assume that the problem is one-dimensional. This is a good approximation for bodies of melt which are sufficiently wide compared to their depth. We also assume that the body is sufficiently deep that the temperature at the bottom remains constant and equal to the temperature when convection ceased. This is equivalent to considering sufficiently early stages of the solidification process, when the cooling effect will not have penetrated to the other side of the body.

3.1. *Temperature field*

As solidification and bubble nucleation occur, there are changes in latent heat. The effect of the latent heat of solidification may be taken into account by modifying the thermal diffusivity in the solidifying region (see Appendix A). Additionally, if the latent heat of vaporization is sufficiently small compared with the latent heat of solidification, it may either be neglected or averaged over the entire solidifying region rather than only at the points of bubble nucleation. This powerful simplification allows the effect of both latent heats to be accounted for by using a modified thermal diffusivity, κ_1, in the solidifying region (see Appendix A).

In the solidifying region, heat diffusion is therefore governed by Fourier's law:

$$\frac{\partial T}{\partial t} = \kappa_1 \frac{\partial^2 T}{\partial x^2}. \tag{3.1}$$

We shall set time $t = 0$ at the moment the melt first becomes quiescent. The temperature of the melt at this time will be uniform at T_o:

$$T = T_o, \quad x > 0, \quad t = 0, \tag{3.2}$$

where x is the distance from the cool solid boundary. For simplicity, we assume that the cooled boundary in contact with the melt remains at the constant temperature

T_b. However, accounting for the effect of latent heat in the solidifying region requires the use of a fictitious boundary temperature T_i, related to T_b (see Appendix A):

$$T = T_i, \quad x = 0, \quad t > 0. \tag{3.3}$$

No condition is specified at $x = 0$, $t = 0$ because of the inherent discontinuity between the initial condition (3.2) and the near-field boundary condition (3.3).

The far-field boundary condition is

$$T = T_o, \quad x \to \infty, \quad t \geqslant 0. \tag{3.4}$$

The solution of (3.1) with the boundary and initial conditions (3.2)–(3.4) is

$$T = (T_o - T_i)\,\mathrm{erf}\left[\frac{x}{2\sqrt{\kappa_1 t}}\right] + T_i, \quad x \geqslant 0, \quad t > 0, \tag{3.5a}$$

$$T = T_o, \quad x > 0, \quad t = 0. \tag{3.5b}$$

3.2. *Concentration of dissolved gas*

Diffusion of dissolved gas through the mushy zone cannot strictly be considered one-dimensional because of the tortuous paths around the crystals. However, for simplicity, we retain the assumption of linear diffusion. We also assume that the chemical diffusivity D is independent of concentration and temperature, and that a constant average value is representative of diffusion throughout the mushy zone.

Diffusion of the dissolved gas is described by Fick's law:

$$\frac{\partial c}{\partial t} = D\frac{\partial^2 c}{\partial x^2} + S, \tag{3.6}$$

where S is a source term accounting for the increase of the concentration of dissolved gas at any point in the mushy zone as a result of crystallization. We account for bubble nucleation separately, as a boundary condition, in the next section. To determine the rate of change of concentration we consider a closed volume V_o, initially free of crystals, containing N moles of dissolved gas. We assume no expansion or contraction on solidification and that the gas is completely insoluble in the solid. When the melt volume is reduced to V by partial solidification, the volume fraction of crystals, f_c, becomes $(1 - V/V_o)$. At any time, the concentration of dissolved gas is $c = N/V$; hence,

$$S = N\frac{\partial(1/V)}{\partial t} = \frac{c}{1 - f_c}\frac{\partial f_c}{\partial t}. \tag{3.7}$$

The relation between the crystal volume fraction f_c and temperature, over an appropriate range, is assumed to be described by a linear function:

$$f_c = -\alpha T + \beta, \tag{3.8}$$

where α and β are constants.

3.3. *Bubble nucleation*

As we are considering bubble nucleation within a crystallizing region, the nucleation of individual bubbles will be predominantly heterogeneous. The concentration and temperature when such heterogeneous nucleation occurs are often determined by modifying the classical theory of homogeneous nucleation. This modification comprises lowering the melt/gas interfacial tension, γ, to account for the presence of the lower-energy solid/melt interface (Kurz & Fisher 1986).

The rate of bubble nucleation J (nuclei per volume per time) is given by (Toramaru 1995)

$$J = \frac{Dc^2}{4m\pi}\sqrt{\frac{k_B T}{\gamma}}(1-(c/c_s)^m)\exp\left\{-\frac{4\pi\gamma}{3k_B T}\left(\frac{2\gamma}{p((c/c_s)^{-m}-1)}\right)^2\right\}, \qquad (3.9)$$

where p is the pressure of the melt, k_B is Boltzmann's constant and m is a constant relating to the gas/melt equilibrium, which has a value of 2 for water as the volatile component. For many melts and for typical temperature ranges, J is a sufficiently strong function of c and weak function of T that the range of c over which nucleation rises from an experimentally negligible level ($\sim$ 1 nucleus $\mathrm{cm^{-3}\,s^{-1}}$) to an instantaneous level ($\sim 10^4\,\mathrm{cm^{-3}\,s^{-1}}$) is very narrow and, thus, is effectively independent of the temperature of the melt (see Appendix B). In this case, the assumption that very rapid, essentially instantaneous, bubble nucleation occurs at a single concentration c^*, independent of temperature, is justified.

Once bubble nucleation occurs, the concentration of dissolved gas in that region is reduced to the saturation concentration c_s at the local temperature. Assuming that there is no kinetic barrier to dissolved gas entering the bubble phase, the concentration of dissolved gas in contact with the bubbles will remain at c_s. Nucleation, therefore, is treated as a boundary condition reducing c instantaneously to c_s and maintaining it at that value.

At time $t = 0$, the fluid has just ceased convecting, and so the concentration of dissolved gas is uniform at c_o:

$$c = c_o, \quad x > 0, \quad t = 0. \qquad (3.10)$$

After the nth burst of bubble nucleation:

$$c = c_s, \quad x = x_n^*, \quad t \geqslant t_n^*, \qquad (3.11)$$

where x_n^* and t_n^* are the position and time of the previous (nth) burst of bubble nucleation.

We consider a sufficiently deep body of fluid such that, at any time, the concentration gradient of dissolved gas will not have penetrated far enough to reach the bottom of the body and hence the far-field boundary condition is

$$c = c_o, \quad x \to \infty, \quad t \geqslant 0. \qquad (3.12)$$

Combining (3.6)–(3.8) gives the equation for the concentration of dissolved gas,

$$\frac{\partial c}{\partial t} = D\frac{\partial^2 c}{\partial x^2} - \frac{\alpha c}{1+\alpha T-\beta}\frac{\partial T}{\partial t}, \qquad (3.13)$$

with boundary and initial conditions (3.10)–(3.12).

3.4. *Solution procedure*

We wish to determine the times and positions of bubble nucleation, at which the concentration of dissolved gas in the melt reaches magnitude c^*. Combining the equation for concentration (3.13) with that describing temperature (3.5) gives

$$\frac{\partial c}{\partial t} = D\frac{\partial^2 c}{\partial x^2} + \frac{\alpha(T_o-T_t)}{2\sqrt{\pi}}\frac{x}{t^{3/2}\kappa_1^{1/2}}c\frac{\exp\left[-x^2/4\kappa_1 t\right]}{1+\alpha(T_o-T_i)\,\mathrm{erf}\left[x/(2\sqrt{\kappa_1 t})\right]+\alpha T_i-\beta}, \qquad (3.14)$$

with boundary conditions (3.10)–(3.12).

To apply boundary condition (3.11), the position and time of the first burst of bubble nucleation, x_1^* and t_1^*, must be specified. It is physically reasonable to assume that the first burst of bubble nucleation should occur at $t_1^* = 0$, as at this time the melt becomes quiescent; the bubbles would form at $x_1^* = 0$, where the melt is at the solid-boundary temperature. Mathematically, however, it is not possible to choose either x_1^* or t_1^* as 0. We shall see later that this is due to the fact that the actual solution tends to a series of geometrically spaced bursts of bubble nucleation, proceeding from $(x, t) = (0, 0)$; hence, there is an infinite number of such bursts within an infinitesimally small distance from the cooled boundary. We need therefore to choose $(x_1^*, t_1^*) \neq (0, 0)$, and also a physically reasonable concentration profile as an initial condition at this time. We have found that the choice of x_1^* and t_1^* does not affect the pattern that the solution settles into after several bursts of bubble nucleation. We also found that the shape of the initial concentration profile had no effect on the long-term pattern of desorption. Indeed, the same pattern was obtained when considering an initial flat concentration profile as well an error function profile. Hence, for mathematical simplicity, we shall specify a uniform concentration beyond a non-zero, arbitrary position at an arbitrary time:

$$c = c_o, \quad x > x_1^*, \quad t = t_1^* \quad \text{where} \quad x_1^*, t_1^* \neq 0. \tag{3.15}$$

Let us introduce the non-dimensional variables

$$C = c/c_o, \quad C^* = c^*/c_o, \quad C_s = c_s/c_o, \tag{3.16a,b,c}$$

$$X_n = x/x_n^*, \tag{3.17}$$

$$\tau_n = t/t_n^*. \tag{3.18}$$

Here, the length scale following the nth burst of nucleation is the distance from the heat sink to this burst, x_n^*, and the time scale is the time at which this burst occurs, t_n^*.

In terms of these new variables, (3.14) may be written

$$\frac{\partial C}{\partial \tau_n} = \frac{D}{\kappa_1}\eta_n^{-1}\frac{\partial^2 C}{\partial X_n^2} + \frac{\eta_n^{1/2}}{2\sqrt{\pi}}\frac{X_n}{\tau_n^{3/2}}C\frac{\exp\left[(-X_n^2/4\tau_n)\eta_n\right]}{\operatorname{erf}\left[(X_n/2\sqrt{\tau_n})\eta_n^{1/2}\right] + \phi}, \tag{3.19}$$

with initial and boundary conditions

$$C = 1, \quad X_1 > 1, \quad \tau_1 = 1, \tag{3.20}$$

$$C = C_s, \quad X_n = 1, \quad \tau_n \geqslant 1, \tag{3.21}$$

$$C = 1, \quad X_n \to \infty, \quad \tau_n > 0, \tag{3.22}$$

where

$$\eta_n = \frac{x_n^{*2}}{t_n^* \kappa_1}, \tag{3.23}$$

The position and time of the first burst of nucleation are now encapsulated in the choice of η_1.

Equation (3.19) contains two dimensionless groupings of physical constants:

$$\phi = \frac{\alpha T_i - \beta + 1}{\alpha(T_o - T_i)} \tag{3.24}$$

and

$$Le^{-1} = \frac{D}{\kappa_1}. \tag{3.25}$$

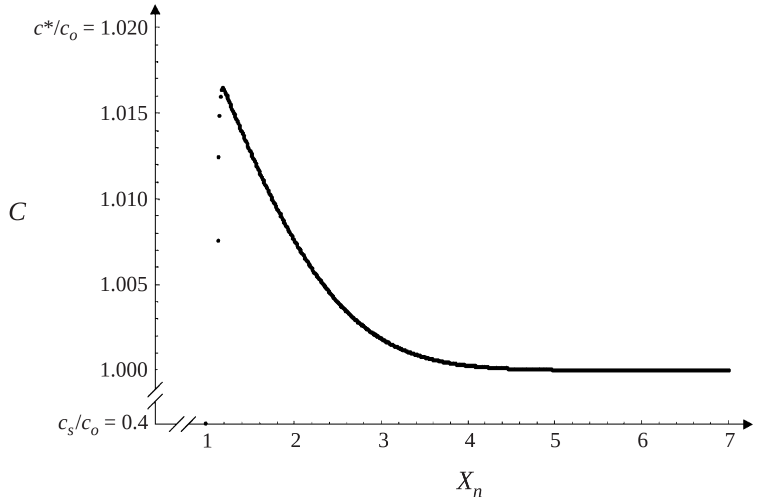

FIGURE 4. Example of a typical concentration profile of dissolved gas between bursts of bubble nucleation, obtained by numerical solution of (3.19).

Equation (3.19) is a second-order parabolic linear differential equation for which an analytic solution could not be found. The equation was solved using an explicit finite difference scheme. The discretizations in space, h, and in time, k, were chosen such that the coefficient $Le^{-1}k/\eta_n h^2$ remained smaller than $\frac{1}{2}$, and hence the solution remained stable (Smith 1985). The characteristic length scale x_n^* and time scale t_n^* increase after each burst of nucleation in such a way that the non-dimensional time and distance between successive bursts of nucleation remain approximately constant. The precision of the numerical scheme and the computing time between each burst of nucleation thus remain the same.

The iterative procedure begins by solving (3.19) for C after the first ($n = 1$) burst of nucleation; η_1 is chosen arbitrarily and the finite difference scheme is marched forward in time until at some point in the X domain, C becomes equal to C^*. At this point, the second burst of nucleation occurs, the concentration C is set immediately to C_s at this position and the solution following the second burst of nucleation is calculated: η_1 is updated to η_2, and the concentration profile at the moment of bubble nucleation is re-scaled and used as the initial condition, in place of (3.20). The finite difference scheme is again marched forward in time until the next burst of bubble nucleation, whereafter the process is repeated. The precision of the solution (as shown by the error bars in figures 6 and 8–12) was estimated using an uncertainty of $\pm h$ and $\pm k$ for x and t, respectively. The convergence of the numerical solution was confirmed by verifying that the solution using finer space and time discretizations lay within the precision of the more coarse result.

4. Model results

Typical concentration and temperature profiles between successive bursts of bubble nucleation are given in figures 4 and 5, respectively. As expected, the concentration of dissolved gas at the previous burst of bubble nucleation, $X_n = 1$, is c_s. Concentration enrichment causes the concentration to rise sharply to a peak within the mushy zone and then decrease gradually to the bulk concentration c_o as $X_n \to \infty$. In contrast, the

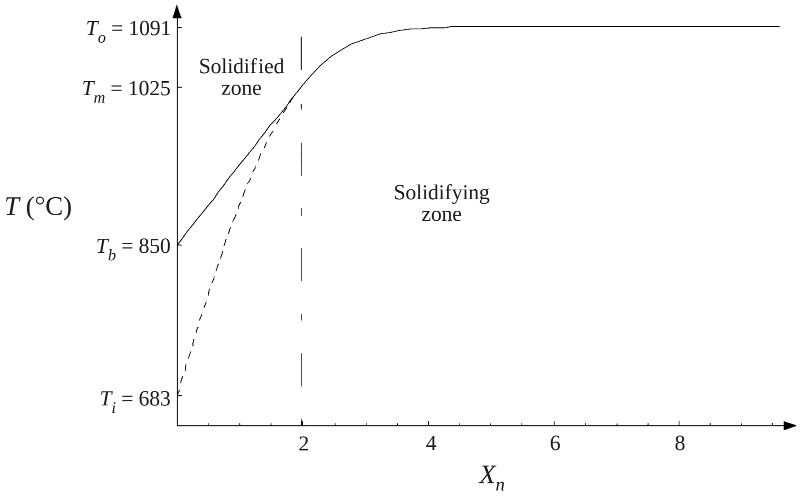

FIGURE 5. Example of a typical temperature profile between bursts of bubble nucleation (solid line). The profile within the solidifying region and its extrapolation (dashed line) was obtained using (3.5*a*).

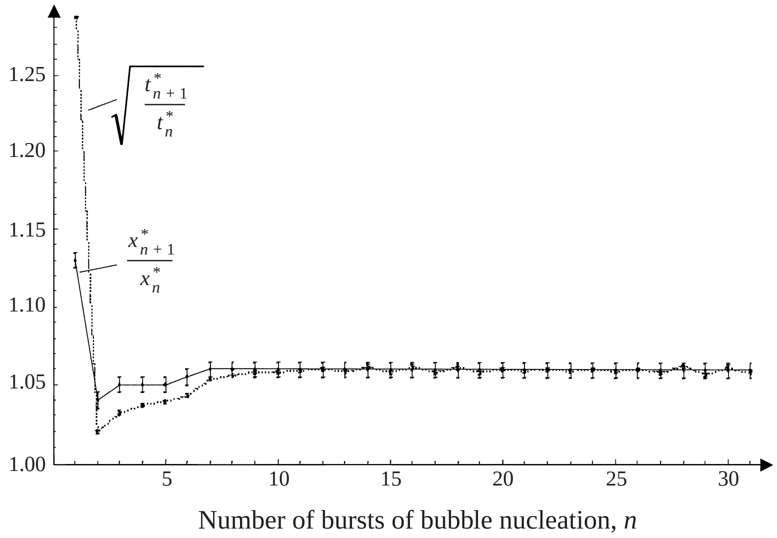

FIGURE 6. A typical evolution of the layer spacing ratio r as the nucleations proceed. The layer spacing becomes more geometrical as the number of bursts of bubble nucleation increases.

temperature (solid line) is influenced only by diffusion, and hence rises monotonically from T_b at the cooled boundary to the bulk temperature T_o as $X_n \rightarrow \infty$. The dashed line in figure 5 shows the extrapolation of the temperature profile within the solidifying zone, given by equation (3.5), to define the fictitious boundary temperature T_i (see Appendix A).

The numerical solution shows that after a number of bursts of bubble nucleation, both the ratio of the times of formation of successive bubble layers and the ratio of the distances from the cooled boundary to successive layers become constant. The number of bursts of bubble nucleation after which the solution converges to this geometric behaviour is determined by the chosen concentration profile at the

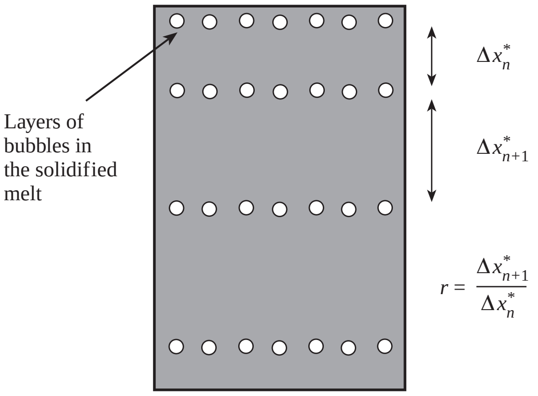

FIGURE 7. A schematic illustrating geometrically spaced bubble layers in a solidified melt.

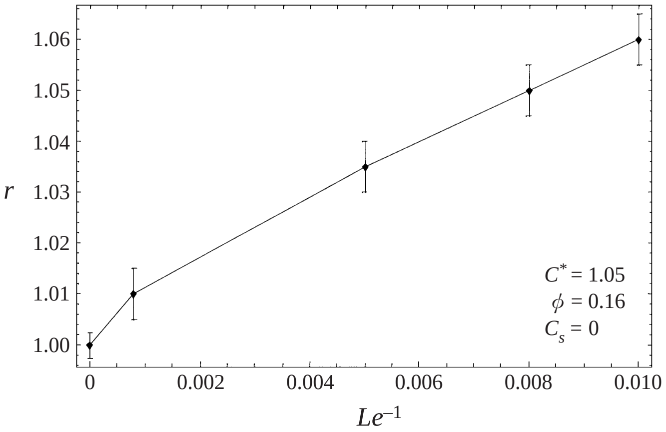

FIGURE 8. The predicted variation of the layer spacing ratio r with the parameter Le^{-1}.

first burst of bubble nucleation and the magnitude of η_1. A typical evolution of the layer spacing ratio as the bursts of bubble nucleation proceed is shown in figure 6. As the number of bursts of bubble nucleation increases, the distance ratio becomes equal to the square root of the time ratio. This result implies that the spacings between successive bubble layers increase in a geometric progression from the cooled boundary, with geometric ratio

$$r = \lim_{n\to\infty} \frac{x_{n+1}^*}{x_n^*} = \lim_{n\to\infty} \sqrt{\frac{t_{n+1}^*}{t_n^*}}. \tag{4.1}$$

A schematic for this pattern is shown in figure 7.

Since the bubbles are predicted to occur in geometrically spaced layers, the pattern of bubble desorption can be described in terms of a single parameter, the layer spacing ratio r. This ratio is therefore a function of the parameters in the model, i.e. $r = r(Le^{-1}, \phi, C^*, C_s)$, and its variation with each of these parameters is plotted in figures 8, 9, 10 and 11, respectively. Figure 8 shows that as the parameter Le^{-1} increases (i.e. as the chemical diffusivity, D, increases relative to the thermal diffusivity κ), the front of dissolved gas depletion can move further from the last site of bubble nucleation x_n^* before it is overtaken by the cooling front to form a new layer of

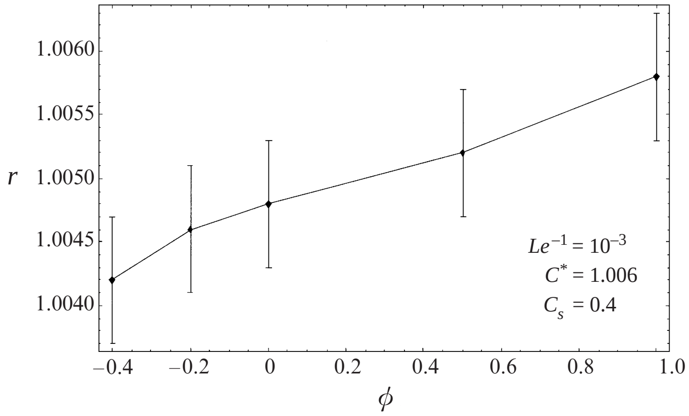

FIGURE 9. The predicted variation of the layer spacing ratio r with the parameter ϕ.

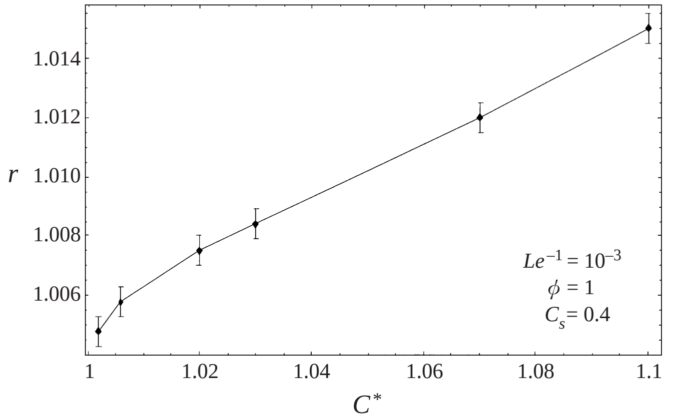

FIGURE 10. The predicted variation of the layer spacing ratio r with the parameter C^*.

bubbles at x^*_{n+1}. Therefore $r = \lim_{n\to\infty} x^*_{n+1}/x^*_n$ increases with Le^{-1}, in accord with our calculations.

The parameter ϕ increases when, for example, the temperature difference between the cooled boundary and the melt $(T_o - T_i)$ is reduced. The progression of the cooling front is slowed and hence, by analogy with the process described above, r increases. This variation is shown in figure 9.

The parameter C^* increases as the concentration at which bubble nucleation occurs, c^*, increases relative to the initial concentration c_o. The concentration of dissolved gas can only reach this higher c^* through greater penetration of the cooling front, as the higher concentration gradient means greater diffusion towards the bubbles. Thus the progression of the gas depletion front will be accelerated whilst the cooling front must penetrate further to achieve bubble nucleation. Therefore r will increase with C^*, as illustrated in figure 10.

Increasing the parameter C_s decreases the driving force for diffusion of the dissolved gas back towards the last site of bubble nucleation. The progression of the gas depletion front is thus slowed and as a result r decreases, as shown in figure 11.

In order to gain insight into the reasons that lead to the formation of geometrically spaced layers of bubbles, let us consider a system without solidification. We consider the diffusion of solute and heat with no source or sink terms in the diffusion equations

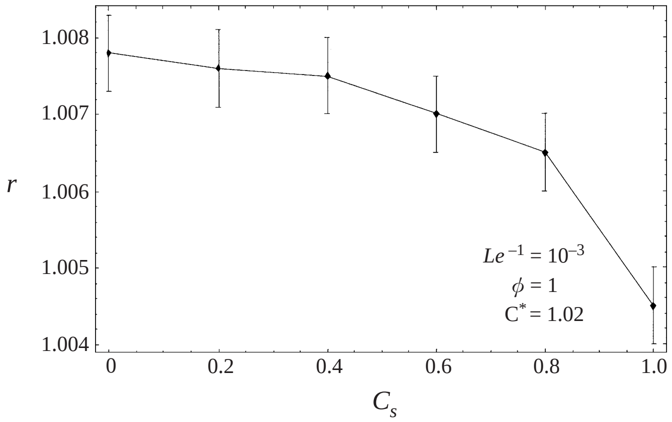

FIGURE 11. The predicted variation of the layer spacing ratio r with the parameter C_s.

(3.1) and (3.6). Bubble nucleation is assumed to occur when the temperature reaches a sufficiently low value T^* and the concentration reaches a sufficiently high value c^*. The non-dimensional position of the point at which $T = T^*$ is $X_n \sim \sqrt{\tau_n}$ and the position of the point at which $c = c^*$ is $X_n - 1 \sim \sqrt{\tau_n - 1}$. When these two positions coincide, bubble nucleation occurs. Since this solution (X_n^*, τ_n^*) is independent of n, geometric layer spacing arises. A similar argument was first presented by Toramaru *et al.* (1996), though those authors recognized, but failed to incorporate, the fixed position of the heat sink in their scaling analysis (Rogerson & Cardoso 1999).

The model described in this report assumes that only $c = c^*$, and not $T = T^*$, is a criterion for bubble nucleation. However, our numerical results show that the concentration of dissolved gas at the point of peak concentration (where nucleation must occur) remains constant, thus implying that bubble nucleation does always occur at the same temperature T^*. Furthermore, the non-dimensional position of the point at which $c = c^*$ is independent of n. Therefore, for the range of parameters studied numerically, we expect a geometric pattern of bubble layering.

5. A physical application

We shall test the validity of our model by comparing its predictions with observations from a large body of solidified rock, the Ogi picrite sill in Japan. This geological formation has been described in Toramaru *et al.* (1996, 1997). A discussion of why the assumptions of this model are appropriate to this physical case is presented in Appendix B.

We must first identify the parameters Le^{-1}, ϕ, C^* and C_s for this physical situation. D/κ is estimated to lie between 10^{-4} and 10^{-3} (Toramaru *et al.* 1996). The incorporation of the effect of latent heat into the thermal diffusivity, that is using κ_1, increases this ratio by a factor of three (see Appendix A). This correction is well within the uncertainty range given above. We have therefore simply considered the range 10^{-4}–10^{-3} for Le^{-1}. The cessation of convection is determined to take place at $f_c = 0.60$, corresponding to $T_o = 1091\,°\mathrm{C}$; T_b is estimated to lie between 850 °C and 950 °C, and α and β are taken as 0.00605 and 7.2, respectively (see Appendix B). The parameter ϕ is then calculated to lie between -0.83 and -0.58. It is assumed that the magma is saturated with water vapour at emplacement and this water is retained in the magma during convection, such that C_s is about 0.4.

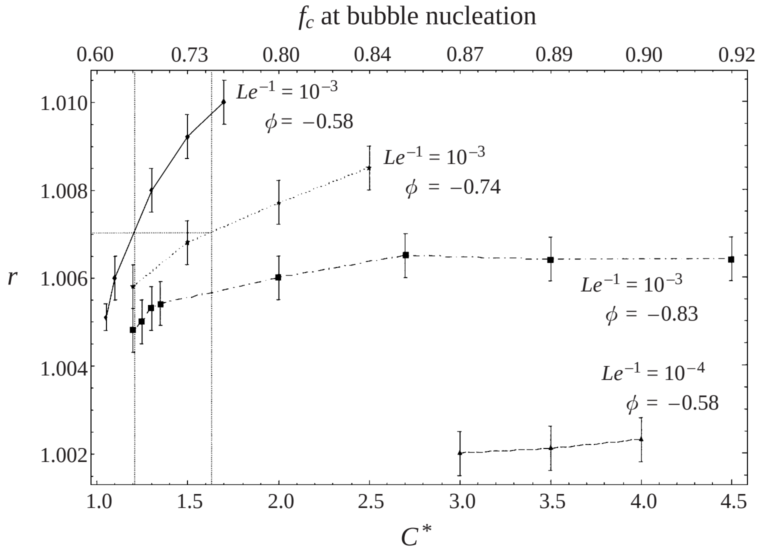

FIGURE 12. The predicted volume fraction of crystals at bubble nucleation in the Ogi picrite sill. $C_s = 0.4$.

The final parameter C^* is difficult to determine because there is insufficient information on the initial concentration of dissolved water vapour in the magma. Also, we do not have a reliable estimate of the gas/melt interfacial tension to allow us to estimate the concentration of dissolved gas at bubble nucleation using (3.9). We shall therefore use the field observations in the model to calculate C^*. We know that a value of C^* will be reasonable if at nucleation there is a sufficiently large crystal volume that bubbles could not then move. Otherwise we would not get the distinctive layers that are observed.

Figure 12 shows the fit of the observed layer spacing ratio of 1.007 in the Ogi picrite sill (Toramaru *et al.* 1997) to the model results over the range of interest, and the predicted crystal volume fraction. The numerical results suggest that both Le^{-1} and ϕ must be sufficiently high within their estimated ranges for the model to predict the layer spacing ratio observed in the field. For $Le^{-1} = 10^{-3}$ and ϕ between -0.58 and -0.74, corresponding to boundary temperatures T_b between 900 °C and 950 °C, the model shows that C^* should have lain within a range corresponding to a crystal volume fraction in the melt of between 0.67 and 0.76 when bubbles nucleated. The crystal fraction at which bubbles are unable to move is dependent on the crystal packing, surface tensions, the size of the bubbles, etc., all of which are not accurately known. However, Toramaru *et al.* (1996) suggest that beyond a fractional crystallinity of about 0.7, bubbles would have been unable to move in the melt. The upper end of the predicted range is therefore consistent with these limited physical results. Indeed, the model does not imply a crystal fraction that is too low or implausibly high. We believe this indicates that the importance features of the physical mechanism of bubble desorption during solidification have been captured in our model.

6. Conclusions

In this contribution, we have developed a numerical model to describe the patterns of bubble desorption during the solidification of a multicomponent melt containing a dissolved gas. Our model considers the one-dimensional cooling of a semi-infinite body of melt. The interplay among cooling, concentration enrichment and diffusion is taken into account.

We showed that the time and location of a burst of bubble nucleation are determined by two competing processes: the advance of the cooling front and the growth of a region depleted of dissolved gas, which grows ahead of the previous nucleation site. This interaction results in a discrete desorption pattern: the bubbles form a sequence of layers parallel to the cooled boundary and the spacing between these bubble layers increases geometrically from the cooled boundary. Our model predicts the dependence of the geometric ratio on the ratio of thermal and chemical diffusivities, on the cooling rate and on the concentration of the dissolved gas at which bubble nucleation occurs. As the chemical diffusivity is increased, in comparison with the thermal diffusivity, the front of dissolved gas depletion moves further from the last site of bubble nucleation before it is overtaken by the cooling front to form a new layer of bubbles, and hence the geometric ratio increases. When the temperature difference between the cooled boundary and the melt is reduced, the progression of the cooling front is slowed and, hence, the geometric ratio increases. As the concentration at which bubble nucleation occurs increases compared with the initial concentration, the progression of the gas depletion front will be accelerated whilst the cooling front must penetrate further to achieve bubble nucleation. Therefore the geometric ratio increases.

We believe that our model captures the important physical mechanisms involved in the solidification and desorption processes by showing that its predictions are consistent with available measurements from a geological formation.

Our modelling approach may be readily extended to describe patterns of precipitation of one component from a multi-component mixture. If the concentration of the component of interest increases as a result of the solidification of lower-melting-point components, then precipitation by concentration enrichment may occur and the situation will be analogous to that presented in this paper.

The authors thank Dr John Lister for helpful discussions as well as Professor Alexander McBirney and Dr Atsushi Toramaru for supplying the reprinted figures. M.A.R. acknowledges the Cambridge Commonwealth Trust and King's College, Cambridge for financial support.

Appendix A. The effect of latent heat

The effect of the latent heat of vaporization, if small, may be taken into account by averaging it over the solidifying solid. The net latent heat per unit mass of solidifying solid is then

$$H = H_{solid} - H_{vapour}e, \tag{A 1}$$

where H_{solid} is the latent heat of solidification, H_{vapour} is the latent heat of vaporization and e is the ratio of the mass of gas to that of solid.

H is included in the governing equation for temperature (3.1) as

$$\frac{\partial T}{\partial t} = \kappa \frac{\partial^2 T}{\partial x^2} + \frac{H}{C_p}\left(\frac{\partial f_c}{\partial t}\right), \tag{A 2}$$

where C_p is the specific heat of the melt and κ is the real thermal diffusivity. Using

(3.8) yields

$$\frac{\partial T}{\partial t} = \kappa \frac{\partial^2 T}{\partial x^2} - \frac{H\alpha}{C_p}\left(\frac{\partial T}{\partial t}\right). \tag{A 3}$$

Hence

$$\frac{\partial T}{\partial t} = \kappa_1 \frac{\partial^2 T}{\partial x^2}, \tag{A 4}$$

where

$$\kappa_1 = \frac{\kappa}{1 + (H\alpha/C_p)}. \tag{A 5}$$

So the effect of the net latent heat H can be expressed by modifying the thermal diffusivity in the solidifying region.

Within the completely solidified layer, however, the normal thermal diffusivity, κ, applies. We therefore seek the solution to the problem of heat diffusion within a body composed of two regions, each with a different thermal diffusivity. The interface between the regions is a free boundary, characterized by its temperature being the solidus temperature and there being continuity of heat flux across it. Crank (1984, pp. 147–149) gives an analytic solution to this problem showing that the temperature in both regions is described by an error function solution of the form (3.5). In this work, we are concerned only with the solution within the solidifying region given by (3.5) with

$$T_i = T_o - \frac{T_o - T_m}{\mathrm{erfc}[\omega/(2\sqrt{\kappa_1})]}, \tag{A 6}$$

where T_m is the solidus temperature of 1025 °C; and the constant $\omega = 1.98$ for $T_b = 850\,^\circ\mathrm{C}$ and 1.16 for $T_b = 950\,^\circ\mathrm{C}$.

For the case of a basaltic magma solidifying at over 1000 °C, water will be exsolved well above its critical point, leading us to believe that the latent heat of vaporization will be very low. In addition, for the low concentrations of water typically dissolved in basalt ($e \sim 0.001$), the contribution of the latent heat of vaporization is negligible compared to that of solidification. Hence, we expect any temperature change caused by bubble desorption to be very small.

For wet basalt, $H_{solid} = 4.2 \times 10^5\,\mathrm{J\,kg^{-1}}$, $C_p = 1.3 \times 10^3\,\mathrm{J\,kg^{-1}\,K^{-1}}$ (Huppert & Sparks 1988*a*) and $\alpha = 0.00605\,\mathrm{K^{-1}}$ (Appendix B) so that

$$1 + (H\alpha/C_p) = 3.0. \tag{A 7}$$

Hence, D/κ should be increased by a factor of three to take into account the effects of the latent heat of both solidification and vaporization.

Appendix B. Application of the model to solidifying magma

A number of observations from the Ogi Picrite Sill (Toramaru *et al.* 1996) suggest that it solidified under conditions similar to those assumed in our model. Indeed, the measurements of the bubble-layer spacings are from a region of the exposed sill where bubble layers are planar, indicating that the temperature gradient was one-dimensional during cooling of that region. The bubbles are observed to have formed in distinct layers implying that bubble movement after nucleation was prevented. The bubble layers are geometrically spaced, suggesting that a concentration gradient was present in the melt and hence convection was negligible. The depth of the exposed part of the sill is of the order of 100 bubble planes and so the assumption of the

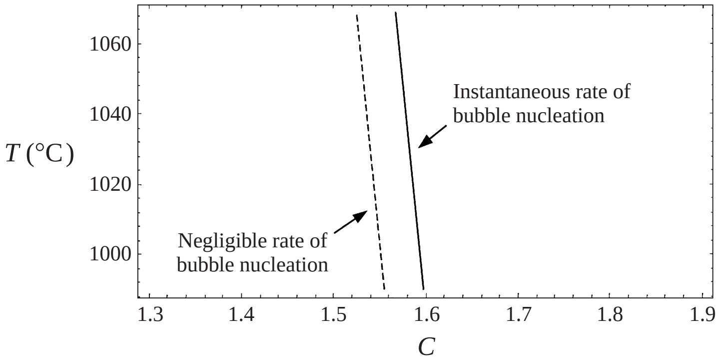

FIGURE 13. Comparison of the conditions of temperature and dissolved gas concentration for which the rate of bubble desorption is experimentally negligible and instantaneous.

sill being infinitely deep is acceptable. The temperature of the surrounding country rock is described by Toramaru *et al.* (1996) as being ‘extremely low’. If we take this temperature as 0 °C, then an inferred estimate for the interface temperature at the cessation of convection, T_b, would be about 600 °C if the roof of the sill did not melt (Huppert & Sparks 1988*b*). We find that this temperature, however, leads to an estimate for ϕ which is too low for the model to be able to predict the field observations. We therefore speculate that a highly insulating foam of desorbed water vapour developed at the top of the sill. These bubbles would have formed when the magma depressurized as it ascended into the sill and buoyancy would cause them to slowly rise through the viscous magma and form the foam. Indeed, Woods & Cardoso (1997) have shown that such foam layer can be tens of metres in thickness, with an thermal conductivity of $\sim 0.1\,\mathrm{W\,m^{-1}\,K^{-1}}$. We find that in this case, T_b could be maintained at about 900 °C during the time required for most of the basalt to solidify. We therefore present numerical results for estimates of the boundary temperature T_b of 850 °C, 900 °C and 950 °C. We also believe that the foam would prevent a chilled layer of basalt forming at the top of the sill before convection ceased. The soft layer of foam would not allow crystals to remain attached and they would be entrained into the bulk by the convective currents. The relationship between the volume crystal fraction and temperature for a basaltic magma is given by Huppert & Sparks (1988*a*) as $f_c = 7200\,T^{-1} - 6$ for $1091\,°\mathrm{C} \leqslant T \leqslant 1200\,°\mathrm{C}$. Neglecting terms higher than first order in a Taylor expansion about $T = 1091\,°\mathrm{C}$ gives $f_c = -0.00605\,T + 7.2$. We extrapolate this relationship to complete solidification at $T_m = 1025\,°\mathrm{C}$.

T_o is taken as the temperature at which the melt undergoes the transition from being quiescent ($Ra < 10^3$) to turbulently convecting ($Ra > 10^6$). Using (2.1) with $\Delta T = T - T_b, d = 40\,\mathrm{m}$ (Toramaru *et al.* 1996), $\kappa = 8 \times 10^{-7}\,\mathrm{m^2\,s^{-1}}$, $\xi = 5 \times 10^{-5}\,\mathrm{K^{-1}}$ and $\nu = 0.1(1 - 1.67 f_c)^{-2.5}\,\mathrm{m^2\,s^{-1}}$ for a basaltic magma (Huppert & Sparks 1988*a*), gives the results in table 1. Over a range of T_b, the transition between the quiescent and turbulently convecting regimes will be quite sharp at $f_c = 0.60$ and $T_o = 1091\,°\mathrm{C}$. Then $\phi = (\alpha T_i - \beta + 1)/[\alpha(T_o - T_i)]$ varies from -0.83 for $T_b = 850\,°\mathrm{C}$, -0.74 for $T_b = 900\,°\mathrm{C}$ to -0.58 for $T_b = 950\,°\mathrm{C}$. Here T_i was calculated as described in Appendix A.

The thermal diffusivities for molten and solid rock are comparable, justifying assuming a single actual thermal diffusivity for melt and solid (Turner, Huppert & Sparks 1986). The effect of using a single average chemical diffusivity and linear diffusion within the crystallizing zone is assumed to be negligible. It is assumed

Ra:	10^3	10^6
$T_b = 850\,^\circ\mathrm{C}$	$f_c = 0.60$ $T = 1091.2\,^\circ\mathrm{C}$	$f_c = 0.59$ $T = 1092.1\,^\circ\mathrm{C}$
$T_b = 900\,^\circ\mathrm{C}$	$f_c = 0.60$ $T = 1091.2\,^\circ\mathrm{C}$	$f_c = 0.59$ $T = 1092.2\,^\circ\mathrm{C}$
$T_b = 950\,^\circ\mathrm{C}$	$f_c = 0.60$ $T = 1091.2\,^\circ\mathrm{C}$	$f_c = 0.59$ $T = 1092.3\,^\circ\mathrm{C}$

TABLE 1. Variation of the temperature and volume fraction of crystals in a basaltic magma during the transition from a quiescent regime ($Ra < 10^3$) to a fully turbulent, convective regime ($Ra > 10^6$). The insensitivity to T_b is also shown.

that the gas is negligibly soluble in the solid and the effect of volume change on solidification or bubble nucleation is negligible.

The assumption of instantaneous nucleation at a constant concentration, independent of temperature, is justified by plotting the nucleation rate predicted by (3.9) as a function of the concentration and temperature of a basaltic magma. We use approximate saturation data of $c_s = 0.1 \times 10^{27}$ molecules m^{-3} ($c = 0.1\%$) at $p = 10$ atm, which is assumed to be independent of temperature. A rough estimate of γ for heterogeneous bubble nucleation is 0.005 N m^{-1} (Sparks 1978) and the chemical diffusivity, D, of dissolved water vapour is about 10^{-10} m^2 s^{-1} (Toramaru *et al.* 1996). The effect of concentration and temperature on the rate of bubble nucleation J (equation (3.9)) are shown in figure 13. The contours of J corresponding to negligible (-1 nucleus cm^{-3} s^{-1}) and instantaneous (10^4 cm^{-3} s^{-1}) rates of bubble nucleation are closely spaced, indicating that C^* (taking $c_o = 0.1 \times 10^{27}$ molecules m^{-3} as mentioned above) varies only between 1.52 and 1.6 over the temperature range 1000 °C–1080 °C.

REFERENCES

CAMPBELL, J. 1991 *Castings.* Butterworth-Heinemann.

CARNEY, D. J. 1953 Gases in liquid iron and steel. In *Gases in Metals.* American Society for Metals.

CRANK, J. 1984 *Free and Moving Boundary Problems.* Oxford University Press.

HUPPERT, H. E. & SPARKS, R. S. J. 1988*a* The generation of granitic magmas by intrusion of basalt into continental crust. *J. Petrol.* **29**, 599–624.

HUPPERT, H. E. & SPARKS, R. S. J. 1988*b* Melting the roof of a chamber containing a hot, turbulently convecting fluid. *J. Fluid Mech.* **188**, 107–131.

KURZ, W. & FISHER, D. J. 1986 *Fundamentals of Solidification.* Trans. Tech. Publications.

MCBIRNEY, A. R. & NOYES, R. M. 1979 Crystallization and Layering of the Skaergaard Intrusion *J. Petrol.* **20**, 487–554.

ROGERSON, M. A. & CARDOSO, S. S. S. 1999 Correction to vesicle layering in solidified intrusive magma bodies: a newly recognized type of igneous structure. *Bull. Volcanol.* **61**, 343–344.

SMITH, D. P. 1985 *Numerical Solution of Partial Differential Equations: Finite Difference Methods.* Clarendon.

SPARKS, R. S. J. 1978 The dynamics of bubble formation and growth in magmas: a review and analysis. *J. Volcan. Geotherm. Res.* **3**, 1–37.

STERN, K. H. 1953 The liesegang phenomenon. *Chem. Rev.* **54**, 79–99.

TORAMARU, A. 1995 Numerical study of nucleation and growth of bubbles in viscous magmas. *J. Geophys. Res.* **100**, 1913–1931.

TORAMARU, A., ISHIWATARI, A., MATSUZAWA, M., NAKAMURA, N. & ARAI, S. 1996 Vesicle layering in solidified intrusive magma bodies: a newly recognized type of igneous structure. *Bull. Volcanol.* **58**, 393–400.

Toramaru, A., Ishiwatari, A., Matsuzawa, M., Nakamura, N. & Arai, S. 1997 Corrections to Vesicle layering in solidified intrusive magma bodies: a newly recognized type of igneous structure. *Bull. Volcanol.* **58**, 655–656.

Turner, J. S., Huppert, H. E. & Sparks, R. S. J. 1986 Komatiites II: Experimental and theoretical investigations of post-emplacement cooling and crystallization. *J. Petrol.* **27**, 397–437.

Wagner, C. 1950 Mathematical analysis of the formation of periodic precipitations. *J. Colloid Sci.* **5**, 85–97.

Woods, A. W. & Cardoso, S. S. S. 1997 Triggering basaltic volcanic eruptions by bubble-melt separation. *Nature* **385**, 518–520.